AGU PUBLICATIONS

JGR

Journal of Geophysical Research: Solid Earth

RESEARCH ARTICLE
10.1002/2013JB010768

Key Points:
- What are the mechanisms of post-seismic (afterslip) creep
- How dynamic fracturing accelerates pressure solution creep
- How healing processes slow down pressure solution creep

Correspondence to:
J. P. Gratier,
Jean-Pierre.Gratier@ujf-grenoble.fr

Citation:
Gratier, J.-P., F. Renard, and B. Vial (2014), Postseismic pressure solution creep: Evidence and time-dependent change from dynamic indenting experiments, *J. Geophys. Res. Solid Earth*, *119*, doi:10.1002/2013JB010768.

Received 14 OCT 2013
Accepted 9 MAR 2014
Accepted article online 15 MAR 2014

Postseismic pressure solution creep: Evidence and time-dependent change from dynamic indenting experiments

Jean Pierre Gratier[1,2], François Renard[1,2,3], and Benjamin Vial[1,2]

[1]ISTerre, Université Grenoble Alpes, Grenoble, France, [2]CNRS, ISTerre, Grenoble, France, [3]Physics of Geological Processes, University of Oslo, Oslo, Norway

Abstract Active faults in the Earth's upper crust can slide either steadily by aseismic creep or abruptly causing earthquakes. Seismic and aseismic processes are closely related: earthquakes are often followed by transient afterslip creep. Postseismic displacement rates progressively decrease with time over a period of years or decades. So seismic fracturing activates the creep rate, and various healing processes progressively reduce it. This article presents pressure solution indenter experiments on halite, calcite, and plaster that show how fracturing and comminution processes induced by dynamic stress loading (applied by dropping steel balls) drastically accelerate the displacement rates accommodated by pressure solution creep by decreasing the dissolution contact area and the diffusive mass transfer distance along this contact. However, as fractures progressively heal and dissolution contacts flatten, these effects disappear, and the displacement rates slow down. The time-dependent change in indenter displacement after dynamic stress loading has been measured and is best fitted by power laws with exponents that change with time from 0.3 to 1 when healing is achieved. Natural postseismic (afterslip) displacement/time relationships have been analyzed and also show a power law change with a power law exponent in the range of 0.25–0.4. It is proposed that the variation in power law exponent with time is related to the change in morphology of the dissolution contact that is fractured or comminuted during the dynamic event and is then progressively healed and smoothed. In natural faults, monitoring the power law parameters could give access to the characteristic healing time in the fault.

1. Introduction

Postseismic transient deformation has been measured on numerous active faults especially since the development of the Global Positioning System and the interferometric synthetic aperture radar techniques in the 1990s [*Chlieh et al*., 2004; *Donnellan et al*., 2002; *Ergintav et al*., 2009; *Hsu et al*., 2006; *Yu et al*., 2003]. In these studies, a fast strain rate, localized mostly in the fault zone, is observed immediately after the earthquake and progressively decreases with time. The associated cumulative displacement after several months is often of the order of magnitude of that of the earthquakes [*Freed*, 2007; *Heki et al*., 1997; *Kreemer et al*., 2006]. Such postseismic deformation has been related to a number of time-dependent processes, including afterslip (slip on the fault itself) [*Freed*, 2007; *Marone et al*., 1991], pore fluid flow (triggered by the earthquake), [*Jonsson et al*., 2003; *Nur and Booker*, 1972], viscous relaxation of the lower crust and upper mantle [*Freed et al*., 2006; *Hetland and Hager*, 2005], brittle creep [*Perfettini and Avouac*, 2004], or pressure solution creep [see, for example, [*Gratier et al*., 2013a], and references therein].

In order to distinguish one type of mechanism from another, the time-dependent change and spatial distribution of the displacement fields produced must be considered [*Feigl and Thatcher*, 2006]. Here the mechanism of afterslip deformation is considered, i.e., slip that occurs in the brittle field of fault zones, in the vicinity of or along seismic ruptures. The afterslip moment inferred from geodetic measurements is frequently several orders of magnitude greater than the seismic moment released by aftershocks [*Barbot et al*., 2009; *Donnellan et al*., 2002; *Yu et al*., 2003]. This implies that the afterslip deformation, which commonly occurs in areas of low seismicity and low coseismic slip [*Hsu et al*., 2009; *Marone*, 1998; *Reilinger et al*., 2000], is often related to aseismic creep processes.

Identifying the mechanisms of aseismic creep along the fault and their change with time is of crucial interest since fault creep relaxes the stress; it also contributes to decreasing the elastic energy stored in fault zones and ultimately the energy liberated during earthquakes.

This study describes a laboratory experiment of dynamic indenting, where a mineral sample, in contact with a reactive aqueous solution, is loaded by a rigid indenter, which is dynamically loaded at regular time intervals. During these experiments, the indenter creep into the sample is measured continuously, and fluctuations in creep rate due to dynamic loading are analyzed.

The experimental results are compared with the observations of natural deformation in fault zones, using microstructural and creep data from the Parkfield area in California, where the San Andreas Fault Observatory at Depth (SAFOD) drilling project [*Zoback et al*., 2010] is located and the postseismic creep data from the Izmit area in Turkey [*Cakir et al*., 2012].

The interest of the SAFOD drilling site is that it provides core samples through both host and fault rocks at 2600 to 2700 m vertical depth within the San Andreas Fault at a transition zone between the 175 km long permanently creeping segment to the north and the seismic segments extending several hundred kilometers to the south along the Parkfield segment and the 1857 Fort Tejon rupture. This allows distinguishing zones of permanent creep from seismic zone with postseismic (afterslip) creep. Permanent creep is accommodated along meter-wide shear zones by a complex combination of creep mechanisms with (i) pressure solution creep involving "solution cleavage to vein" diffusive mass transfer [*Gratier et al*., 2011] and (ii) a granular-type flow mechanism involving frictional sliding of low-temperature phyllosilicate minerals [*Carpenter et al*., 2011; *Holdsworth et al*., 2011; *Lockner et al*., 2011] coupled with stress-driven diffusive mass transfer at the grain boundaries of rigid-soluble minerals and clast aggregates (quartz, calcite, and feldspars) [*Hadizadeh et al*., 2012; *Richard et al*., 2013].

To the south, the seismicity evolves from the Parkfield segment, a zone of successive *M*6 earthquakes immediately south of the SAFOD site, to a locked segment with *M*8 earthquakes (i.e., *M*7.9 1857 Fort Tejon). The last *M*6 Parkfield event induced discontinuous surface breakages that propagated from the south to several kilometers north of the SAFOD site [*Langbein et al*., 2005] and was followed by postseismic (afterslip) creep [*Freed*, 2007]. Evidence of coseismic rock damage and postseismic healing of the fault zone have been recorded [*Li et al*., 2006]. These changes occurred throughout the damaged zone in the upper crust with a maximum change in the zone of maximum seismic slip. The measured rigidity recovery, most likely due to the closure of cracks that opened during the main shock, occurred with a healing rate that decreased with time simultaneously with the decrease in postseismic displacement rate [*Brenguier et al*., 2008]. The great *M*7.9 Fort Tejon event is thought to have propagated through Parkfield [*Sieh*, 1978]. Consequently, it is likely that there could be some evidence of co and postseismic processes in the SAFOD samples. Episodic cataclastic deformation is easily identified on samples from the damaged zones retrieved from SAFOD as (i) repeated cycles of cataclasis, pressure solution creep, and fluid pressure-induced fracturing processes [*Bradbury et al*., 2011; *Hadizadeh et al*., 2012; *Holdsworth et al*., 2011; *Janssen et al*., 2011; *Schleicher et al*., 2009]; (ii) episodic fluid flow events with metasomatic reactions [*Holdsworth et al*., 2011; *Mittempergher et al*., 2011; *Moore and Rymer*, 2012; *Schleicher et al*., 2009]; and (iii) episodic sealing of open fractures by euhedral crystals [*Mittempergher et al*., 2011]. Also of interest is the resetting of the feldspar thermoluminescence, 139 years before 2010 as described by [*Spencer et al*., 2012] and that could have been related to the *M*7.9 1857 Fort Tejon earthquake. So there is a lot of evidence of episodic cataclastic events in the SAFOD samples. Some of these events could be related to the microseismicity that is permanently observed in the creeping zone [*Nadeau et al*., 2004], but others could also be related to larger earthquakes. The identification of the parameters of deformation processes associated with such episodic events, namely, creep, fracturing, and healing processes, is crucial as these processes may well have been associated with aseismic afterslip creep.

The mechanisms and the time-dependent change in the fault rock behavior are investigated in this context, using laboratory experiments to characterize the effect of both fracturing and healing on the kinetics of creep processes. These dynamic indenter experiments, reproducing postseismic deformation in the laboratory, are interpreted with reference to the observations of naturally deformed samples at depth and to observed postseismic (afterslip) deformation in two active faults after earthquakes (the 2004 *M*6 Parkfield and the 1999 *M*7.2–7.4 Izmit earthquakes).

2. Dynamic Indenting Experimental Method

The principle of static indenter experiments is to load a rock or a mineral sample in contact with its saturated solution with a rigid indenter, bearing a constant dead weight, for a period of several weeks to months

[*Dysthe et al*., 2002; *Gratier*, 1993; *Hickman and Evans*, 1991; *Karcz et al*., 2008; *Tada and Siever*, 1986]. The difference in normal stresses between the sample surface in contact with the indenter and its free surface away from the indenter promotes a difference in chemical potential that drives diffusive mass transfer through the fluid phase trapped under the indenter toward the free fluid phase around the indenter [*Paterson*, 1973; *Rutter*, 1976; *Weyl*, 1959]. The displacement rate is proportional to the solubility of the solid in its solution. The indenter displacement is monitored in order to quantify the kinetics of such stress-driven mass transfer process, which is always slow due the very low thickness (i.e., nanometer) of the trapped fluid phase [*Gratier et al*., 2009]. Consequently, long-duration experiments are always required even in the best conditions of a high-solubility solid in contact with an aqueous solution.

Local mass transfer processes below and around the indenter are also driven by elastic and/or plastic strain energy gradients near the indenter induced by the static load [*Karcz et al*., 2008; *Tada and Siever*, 1986]. In this case, diffusive mass transfer occurs through the free fluid surrounding the contact under stress, so it is much faster than diffusive mass transfer along the fluid phase trapped under stress. However, this strain energy thermodynamic driving force remains a secondary effect if the solution is well saturated before the experiment [*Gratier*, 1993; *Hickman and Evans*, 1991] and if the fluid volume around the indenter is kept as small as possible [*Dysthe et al*., 2003]. This effect is negligible on the displacement rate of the indenter when compared to the thermodynamic driving force due to the difference in normal stress [*Gratier et al*., 2009]. The advantage of the indenter technique is that it allows the same transfer path geometry to be maintained throughout the experiment. So it is well adapted to the study of the kinetics of stress-driven mass transfer creep (i.e., pressure solution creep), which is highly sensitive to the diffusive path transfer distance [*Raj*, 1982; *van Noort et al*., 2008].

In the present work, a new technique is used: dynamic indenting experiments, which are performed in order to reproduce the interactions between fracturing and healing on creep processes (Figure 1). The dynamic effect is obtained by letting a steel ball drop on the dead weight that loads the indenter. This dynamic perturbation is produced from time to time (weeks or months) and induces dynamic fracturing and comminution processes that are considered to reproduce the damage created during an earthquake. Then, the microfractures heal, and the dissolution contacts flatten, thanks to the stress-driven mass transfers associated with pressure solution creep.

Experiments have been performed on various minerals such as halite, plaster, and calcite at 40°C and under atmospheric fluid pressure. The procedure is the same for all experiments (Figure 1): a cylindrical sample (1 cm diameter and 0.5 cm height) is placed into a cell. Then, a solution previously saturated with the mineral at the temperature of the experiment is poured on the sample. The volume of the solution is controlled to be as low as possible, usually well below the volume of the sample (Figure 1). An indenter is loaded on the sample and three high-resolution displacement sensors (linear encoders and Solartron interferometer, with less than 0.5 μm accuracy) are fixed at angles of 120° around a circle centered on the indenter, ensuring that the average value of the three displacement measurements corresponds to the vertical displacement of the indenter. Then, a layer of low-viscosity liquid paraffin is poured around the indenter on the saturated solution to prevent it from evaporating (Figure 1). Finally, the required dead weight is loaded on the indenter, which sets the time zero of the experiment. The displacements are recorded at a rate of one measurement every 20 min. Up to 12 experiments are run simultaneously, and the whole experimental setups are placed in ovens maintained at a controlled temperature of 40°C. Some days or weeks are required, depending on the nature of the sample, in order to obtain a stabilized displacement rate. Then from time to time, a steel ball with controlled weight (from 28 to 80 g) is dropped on the dead weight from a given height (13 cm). To determine long-term effects, experiments are run for several months (up to 300 days). The effects of several parameters on the indenter displacement over time have been studied: nature of the mineral, chemistry of the solution, weight of the ball, and shape of the indenter (see Table 1). The first two parameters are included in the creep laws. Using various ball weights allow investigating the range of dynamic forces that could modify the creep rate.

Finally, after the experiments, the samples were characterized using various imaging techniques: optical microscopy, cathodoluminescence, and scanning electron microscopy. One sample (plaster) was also imaged using X-ray computing microtomography to search for the adsorption contrast in the zone below the indenter. This was performed at the Swiss Light Source synchrotron facility, at a voxel resolution of 5 μm^3.

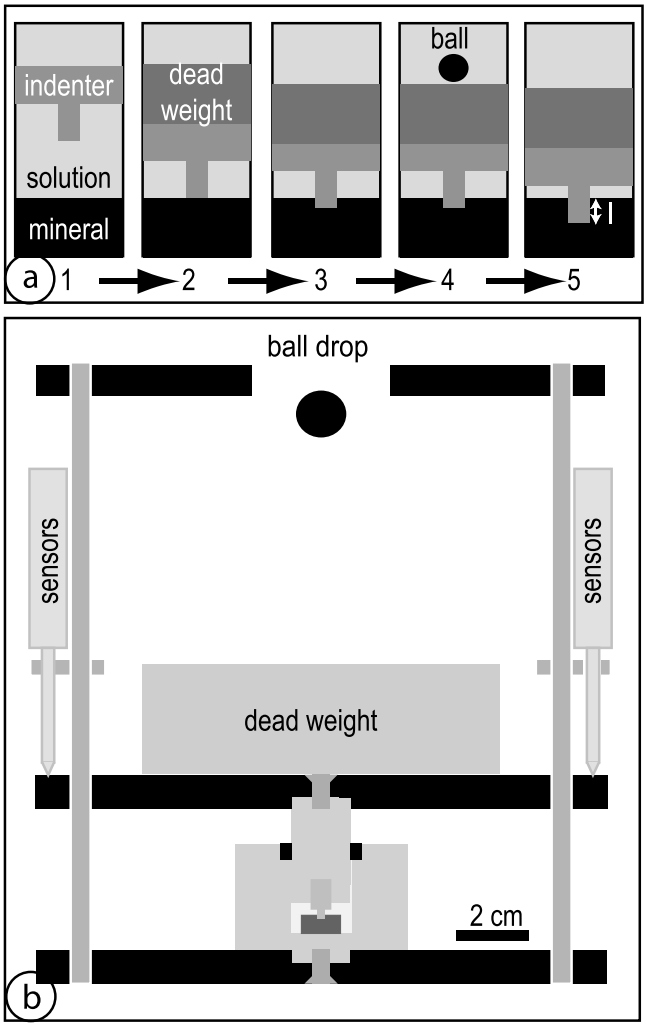

Figure 1. (a) Experimental setup: (1) sample in contact with a saturated solution, (2) indenter in contact with the sample and static loading (dead weight), (3) static indenting, (4) dynamic loading (drop ball), and (5) post-shock indenting. (b) Apparatus for the dynamic indenter technique: the sample (dark gray) is surrounded by a saturated solution (light gray), and the container is sealed by paraffin (black); the dead weight, the dropping ball, and the three displacement sensors for measuring the rate of indentation are also shown.

3. Results

3.1. General Observations Before Any Shock

Prior to dropping the ball, a nonlinear change in the displacement versus time curves was always observed as in other experiments [*Dysthe et al*., 2002]. The experiments were continued for several weeks (600 to 1100 h; Figure 2) with slowly decreasing indentation rate before the first shock. The effect of the following key parameters gives information on the mechanism of deformation.

1. *Presence of solution and solubility of the solid in its solution*: For experiments performed without any solution (dry condition), no measurable displacement was obtained when using the same stress as with a solution. For the three minerals tested: halite, plaster (gypsum mineral: $CaSO_4$ $(H_2O)_2$), and calcite, an aqueous solution was used that was saturated before the experiment at the same pressure and temperature conditions as those of the experiments. Moreover, for calcite NH_4Cl, 1M solution was used that increases the solubility of the solid in solution [*Ikornikova*, 1961]. In this case (Figure 2), the displacement rate before the first shock was faster with the higher-solubility values: 19 μm in 500 h with NH_4Cl 1M solution compared to 8 μm in 500 h with an aqueous solution.

Table 1. Test Parameters: Nature of Samples and Saturated Solutions, Diameter of Indenters, Static Stress on Indenters, and Temperature of Experiments

Sample	Saturated Solution	Indenter Diameter	Stress on Indenter	Temperature
Plaster A	Water	2 mm	3 MPa	40°C
Plaster B	Water	2 mm	3 MPa	40°C
Plaster C	Water	2 mm	3 MPa	40°C
Plaster D	Water	2 mm	3 MPa	40°C
Halite A	Brine	0.5 mm	48.6 MPa	40°C
Halite B	Brine	0.5 mm	48.6 MPa	40°C
Calcite A	Water	0.4 mm	146.8 MPa	40°C
Calcite B	NH_4Cl 1M	0.4 mm	146.8 MPa	40°C

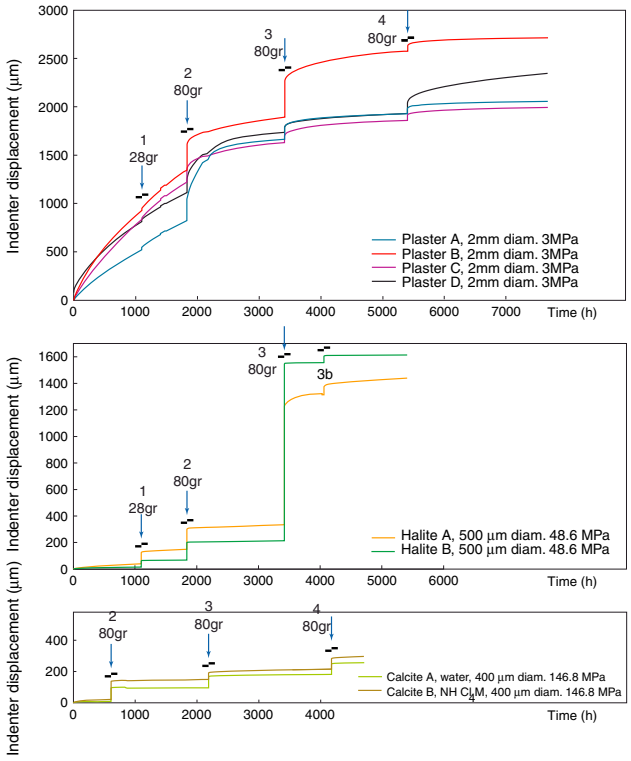

Figure 2. Displacement of the indenter versus time for the various samples: plaster, halite, and calcite. The static stress value (imposed by the dead weight), the saturated solution, the indenter diameter, the time of the various shocks (arrows) induced by the dropping ball, and the weight of the ball are indicated. The events on halite at step 3b were not triggered by a direct shock.

2. *Indenter diameter*: Ceramic cylindrical indenters were used, the same size for each set of samples; therefore, it was not possible to test directly the effect of the indenter diameter. However, on several occasions, the indenter broke under the effect of the dropping ball. This breakage was useful for testing the effect of the size of the contact area, since it shifted the contact surface area from that of the indenter (some hundred micron diameter) to that of its base (some millimeter diameter). This happened only for crystal halite, and the increase in contact surface area always prevented the indentation from continuing. This indicates that the displacement rate is roughly inversely proportional to the contact surface area of the indenter, as commonly observed in previous studies [*Gratier et al.*, 2013a].
3. *Sample porosity*: Granular samples with high porosity always deformed much faster than crystalline samples without porosity. This is clearly the case when comparing the behavior of plaster (~40% porosity) with halite single-crystal samples (0% porosity). Despite the fact that the solubility of halite is about a hundred times higher than that of the plaster, the displacement rate is always faster for the porous plaster aggregate, for example, more than 20 times greater in Figure 2 when comparing the fastest displacement rate of halite and plaster samples after 1000 h: 37 and 900 μm, respectively. This difference may be related to the effect of the contact surface area as suggested above, since the difference in porosity implies a difference in size of the stressed contact surfaces, which is the size of the indenter for halite (several hundred micrometers) and the size of the grain contacts for the plaster aggregate (a few micrometers).
4. *Stress*: The permanent stress imposed by the dead weight on the indenter was adapted to the strength of each sample, in order to remain well below the yield strength (60–70%). For each mineral, a constant stress value was used: 3 MPa for plaster, 48.6 MPa for halite, and 146.8 MPa for calcite, in order to test the reproducibility of the experiments. With all experimental conditions being the same (temperature, stress, indenter size, and aqueous solution), the displacement rates show a wide variability, ranging, for example, from 620 to 900 μm/1000 h for plaster and from 11 to 37 μm/1000 h for the halite. Such a spread in creep rates had already been observed in other experiments of pressure solution indenting [*Gratier et al.*, 2009].

3.2. Aftershock Displacements

The representative effect of the dropping ball on the displacement rates for the three minerals is shown on Figure 2.

For plaster, four shocks were imposed: the first with a small weight (28 g) and the other three with a larger weight (80 g), with the same fall height (13 cm). The first shock induced only a small change in the displacement versus time relationship. The other three induced a substantial increase in displacement rate, up to 10 times greater, for example, shifting from 0.3 to 3 μm/h. Then, after each shock, the displacement rate progressively decreased. Note that, for each sample, the nearly stabilized displacement rate that was

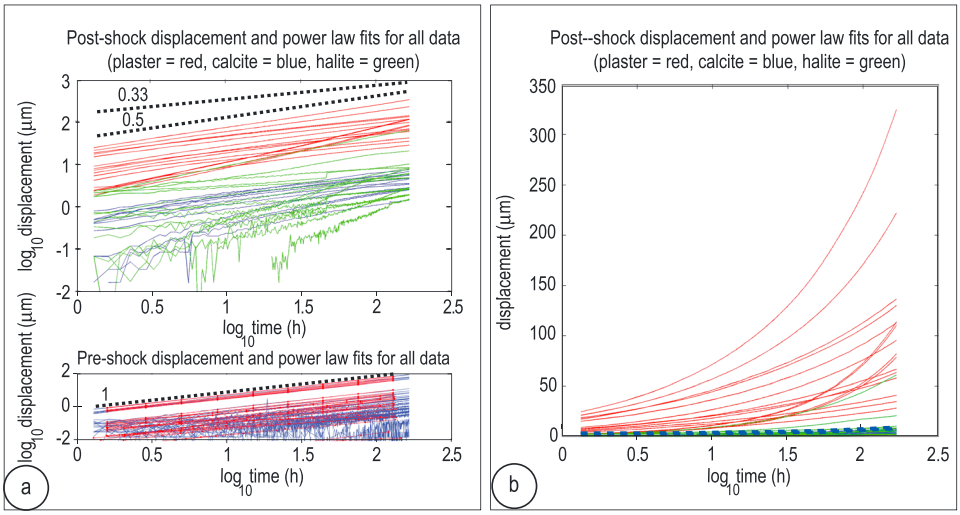

Figure 3. (a) Log-log plot of the displacement of the indenter versus time showing a power law for the postseismic displacement for a 100 h window of time and the linear relation for the same preshock period (100 h), after either static deformation or long-duration postseismic healing (see Figure 2). (b) Semi-log plot of the same postshock displacement versus time curves indicating that the curves do not show logarithm dependence.

established 2 to 3 months after the shocks decreased after each shock for three cases out of four. In one case (D) only, the nearly stabilized displacement rate after the third shock is higher than after the preceding shocks. The cumulative displacement versus time curves also show the differences in the amount of coshock displacements.

For halite, only three shocks were imposed, as the third one induced a very large displacement. The first shock used a ball of lighter weight than the other two. However, in this case, its effect was virtually the same as that for the second shock. Note that a change in displacement rate occurred without any shock imposed on the dead weight (two events in parallel = 3b in halite, see Figure 2). This may have been induced by an unidentified man-made or natural effect. In all cases, the displacement rate increased drastically after the shock, but the recovery time was much shorter than the value found for the plaster, except after one shock for sample A in Figure 2.

For calcite, the three shocks imposed used the same ball weight. Note that, in this case, the postshock displacement rates are rather low, and, as was the case for halite, the recovery time was much shorter than for plaster.

The characteristics of the displacement versus time relation were deduced from log-log and semilog plots for a given time window (100 or 200 h). Figure 3 shows the data for all the experiments.

3.3. Observation of the Deformed Samples

A distinction must be made between the fracturing and deformation patterns below the indenter for granular cohesive porous (plaster) and crystalline nonporous (halite and calcite) samples.

On nonporous samples, the shocks lead to three different effects: (i) radial fractures initiating from the center of the hole, (ii) comminution process below the indenter, and (iii) reversed crown-shaped fractures around the hole that are detailed below.

1. Radial fractures are seen nucleating from the center of the hole, where the stress is highest. They initiate as open cracks (Figure 4a) that then progressively heal (Figure 4i) or seal (Figures 4b–4e) during the postshock period. Two mechanisms can be inferred: a self-healing process driven by the minimization of the surface energy of the crack surface [*Kingery et al.*, 1976; *Smith and Evans*, 1984] and a stress-driven dissolution and redeposition process where the dissolution products below the indenter seal the fractures.
2. A comminution process is seen below the indenter, for example, for halite (Figures 4c and 4d) leading to the formation of a rough contact surface after the shock on the indenter. This rough surface progressively flattens during the dissolution process (Figures 4f and 4g).

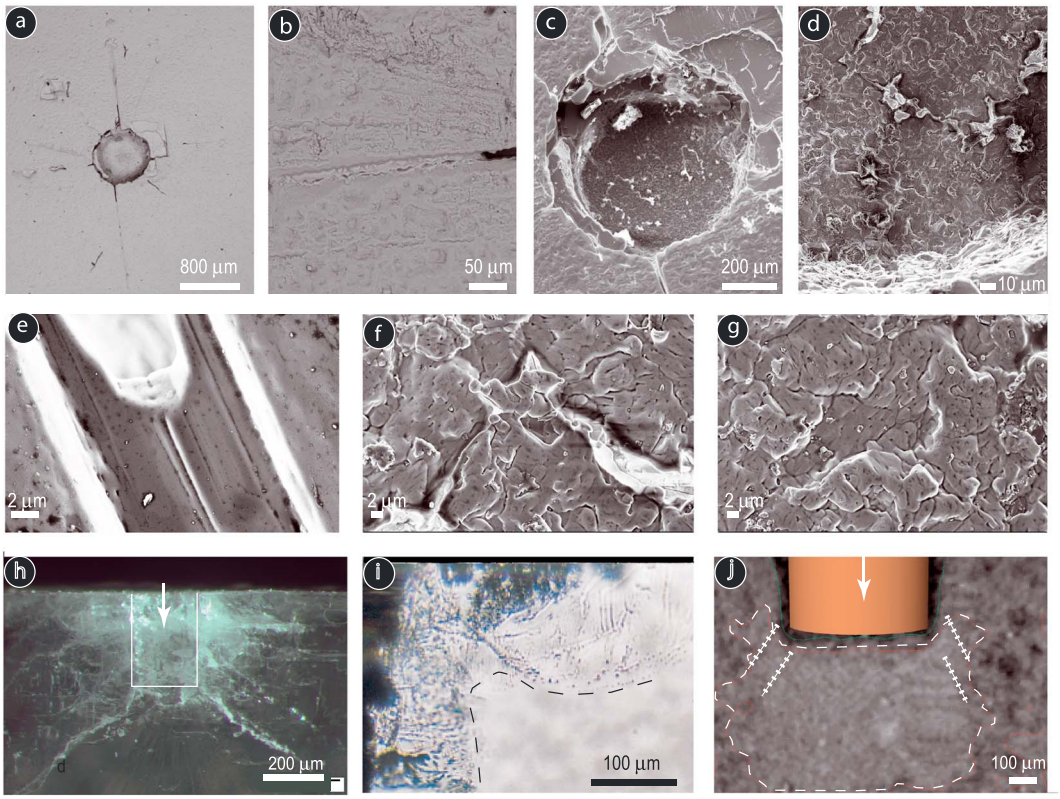

Figure 4. Images of the samples after dynamic loading, followed by postshock displacement and healing. (a) Axial view showing the network of healed and partially sealed radial fractures. (b) Fracture sealing by halite deposition in the fracture. (c and d) Roughness of the sample surface at the contact between the indenter and the sample. (e) Detail of the sealing of the fracture around the indenter by successive layers of deposition. (f) Detail of the sealed fracture below the indenter. (g) Detail of the halite surface below the indenter. (h) En-echelon reversed crown-shaped fractures rooted at the corner of the indenter (open white rectangle shows the location of the indenter). (i) Healed fractures (revealed as cloud of fluid inclusions) in halite. (j) Zone of compaction below the indenter in plaster revealed by X-ray microtomography, the lighter the color, the higher the porosity; the dashed line underlines the boundary of the damaged zone; the dotted lines highlight the en-echelon reversed crown-shaped fractures. The arrows indicate the indenting direction. Figures 4a–4i represent halite, while Figure 4j represents plaster.

3. En-echelon reversed crown-shaped fractures are seen under the hole (Figure 4h). However, it is not clear if these fractures are associated with the shock, since they are also seen in static indenting experiments [*Gratier et al*., 2009].

On porous samples, the same radial fracture network and comminution process below the indenter are seen in axial view (Figure 5a). The difference is that the comminution process is also associated with a decrease in sample porosity below the indenter (with a thickness that is of the order of magnitude of the indenter diameter, see Figure 4j) first by an instantaneous (coshock) cataclastic process and progressively by pressure solution compaction. The initial state of the plaster can be seen in Figures 5b and 5c. The deformed state is shown in Figure 5d (with a view of the indenter contact) and in Figures 5e and 5f (with clear pressure solution indenting in this last view). En-echelon reversed crown-shaped fractures are also seen (Figure 4j) with the same question being raised concerning their development timing, just like the nonporous samples: during the shock or between the shocks?

4. Discussion

4.1. Indenting Mechanism

The observations of the samples (Figures 4 and 5) show that the depth of the holes formed underneath the indenters by a dissolution process depends on the presence of a solution and the solubility of the solid in a solution (Figure 2): such features indicate that the indenting mechanism is a stress-driven mass transfer

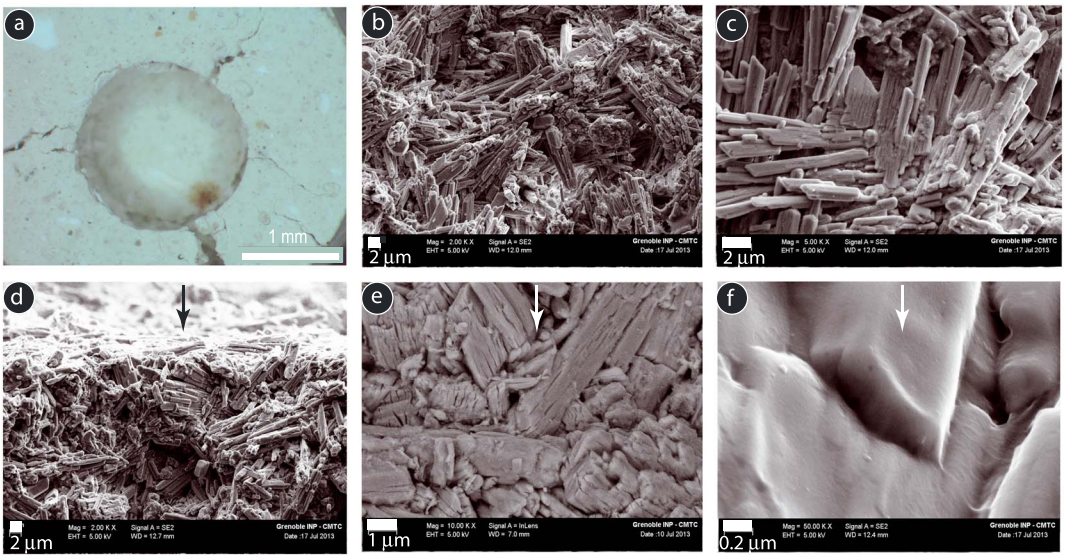

Figure 5. View of the plaster samples after dynamic loading, followed by postshock displacement and healing: (a) Axial view showing the network of radial fractures; (b and c) initial state of the plaster, away from the indenter, view perpendicular to the indenting direction, and deformed state of the plaster, with a view of the (d) indenter contact surface, (e) grain compaction, and (f) pressure solution indenting of two grains. The arrows indicate the indenting directions.

process, namely, pressure solution creep. In such case, according to theoretical models [*Paterson*, 1973; *Rutter*, 1976; *Weyl*, 1959], the displacement of the indenter should be proportional to the solubility of the solid in solution, the molar volume of the solid, the product of the diffusion coefficient along the indenter-sample interface by the thickness of the fluid phase, and the driving stress, which, in this case, is the difference between the axial normal pressure imposed by the indenter and the atmospheric fluid pressure [*Rutter*, 1976].

The dependence of the creep rate on the distance of mass transfer along the fluid phase trapped under stress is related to the rate limiting process. Pressure solution along a stress contact is a three-step process: dissolution, followed by diffusion, and then redeposition. If one of these steps is much slower than the other, it imposes its kinetics on the entire creep process [*Rutter*, 1976]. The indenter displacement rate ($\Delta l/\Delta t$) is inversely proportional to the square of the mass transfer distance (d); here either the diameter of the indenter (crystalline sample without porosity) or the diameter of the grain contact (with granular porous or comminuted crystalline samples) if the whole process is diffusion limited. The $\Delta l/\Delta t$ does not depend on d for reaction limited pressure solution creep (dissolution or redeposition). The creep rate is linearly dependent on stress at low driving stress values [*Rutter*, 1976] and becomes exponentially stress dependent at higher stress values [*Gratier et al*., 2009].

In previous static indenting experiments on halite (with near flat crystalline surface without any comminution), where the effect of indenter diameter was tested [*Gratier*, 1993], the observations of this indenter diameter effect, with displacement that drastically decreases with increase in indenter diameter, were interpreted to be indicative of a diffusion-limited process.

4.2. Effect of Fracturing and Comminution Processes

The effect of the shocks due to dynamic loading is to drastically increase the displacement rate (Figure 2). Among the parameters of the creep law previously discussed, only the geometry of the indenter-sample interface is modified by the shocks that induce fracturing and comminution. The shocks promote radial fracturing below the indenter (Figure 4a). As the thickness of the fluid phase trapped under stress below the indenter is much smaller (nanometers) than the thickness of the fracture (a few microns), and when the fracture lengths are greater than the indenter diameter, the fracture network provides a shortcut for the diffusion process as the diffusive flux along the fracture (product of the diffusion coefficient by the thickness of the diffusion path) is a thousand times higher than the diffusive flux through the trapped fluid phase. Consequently, the mass transfer distance changes from the indenter diameter (d), before the shock, to the

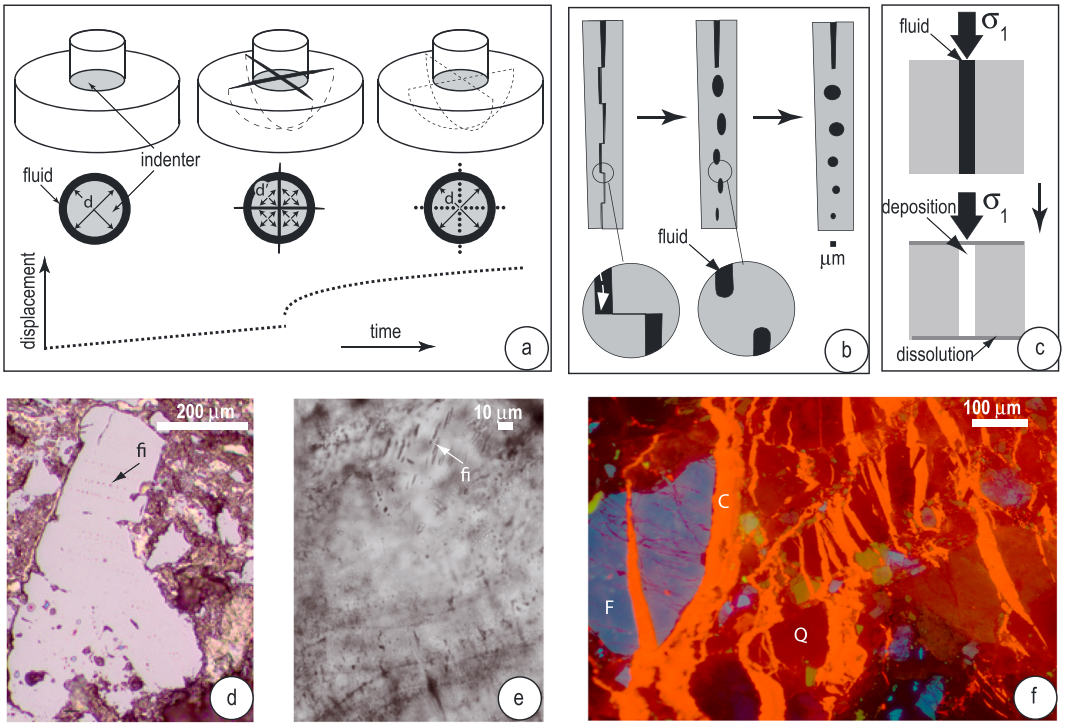

Figure 6. Postshock mechanisms of fracture healing and sealing: (a) from left to right, preshock, shock, and postshock structures in parallel with the time-dependent variation in displacement. The displacement rate ($\Delta l/\Delta t$) is inversely proportional to the square of the mass transfer distance (d before the shock and d' after the shock). (b) Healing of fracture driven by minimization of surface energy. (c) Stress-driven mass transfer (pressure solution) that accommodates both the indenter displacement and the fracture sealing. (d and e) Healed and (f) sealed fractures in the natural sample (SAFOD samples in the damaged zones).

spacing between fractures (d') after the shock (Figure 6a). As the displacement rate is inversely proportional to the square of the mass transfer distance, the drastic decrease in mass transfer distance immediately increases the indenting displacement rate.

The comminution process induced by the shocks at the contact between the indenter and the sample contributes to this nonlinear effect as the dissolution surface is rougher after the shock (Figures 4c and 4d) than before (initial state is seen on Figures 4a and 4c, away from the indenting area), for example, for halite. As a result, the dissolution contact area after the shock is much smaller than the indenter diameter (see schematic view in Figures 7a, step 1 and 7b, step 3), so the displacement rate is much faster due to the decrease in mass transfer distance and to the increase in stress, which is imposed by the constant dead weight. Such a roughening effect has already been observed during a single-contact pressure solution creep on undeformed salt [*Dysthe et al.*, 2003; *Karcz et al.*, 2006]. Moreover, for granular cohesive plaster sample, a damaged zone is observed below the indenter, its thickness being of the same order of magnitude as the indenter diameter (Figure 4j). Consequently, the comminution process drastically reduced the contact surface area (Figure 7a, step 3), and because the displacement rate is inversely proportional to the dissolution contact area, the displacement rate after the shock increased significantly.

Consequently, radial fracturing and comminution led to a drastic acceleration of the creep rate, as the mass transfer distance is reduced along the fluid phase trapped under stress and the stress increases. Note that the reverse crown-shaped fracture does not change the contact geometry and so may have a minor effect on the creep rate, as already discussed for static indenting [*Gratier et al.*, 2009].

4.3. Effect of Fracture Healing and Sealing

Immediately after being activated by the shocks, the displacement rate starts decreasing (Figure 2). Postexperiment observations show that the fractures are healed and sealed during the period between two

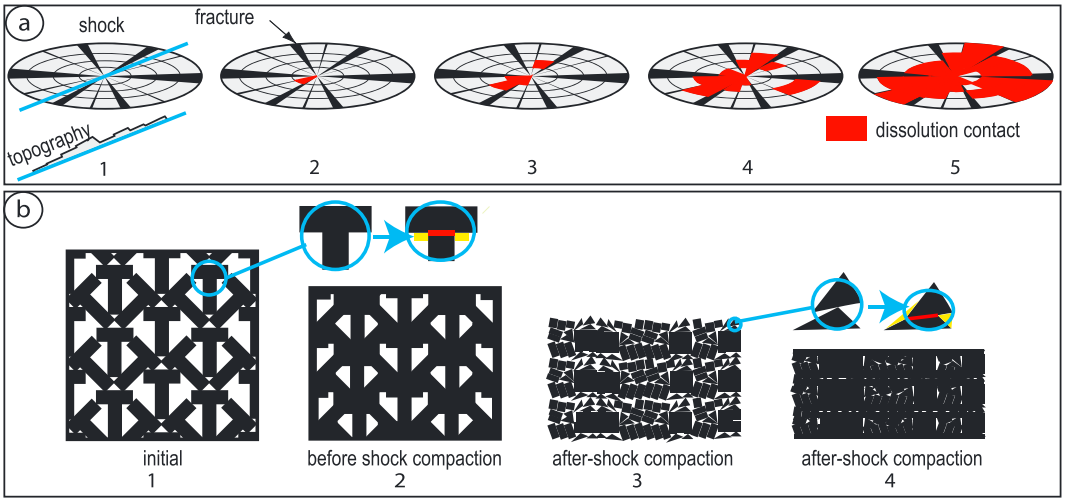

Figure 7. Postshock change in the roughness of the dissolution contact and the porosity below the indenter: top = perspective view of the surface of dissolution with a cross section of its topography (below step 1); bottom = cross section of the deformed sample near the dissolution surface. (a) Change in surface area of dissolution (red) after a shock. The topography is schematically represented along a cross section (blue) at the step of the shock (step 1). The surface area of the dissolution contact increases, leading to the decrease of the displacement rate of the indenter (steps 2 to 5). Dissolution contacts are underlined in red, while free fluid in fracture are black. (b) Variation in porosity below the indenter in a plaster sample, steps 1 and 2 static indenting, steps 3 and 4 shock and aftershock compactions. Dissolution contacts are underlined in red, redeposition in yellow, plaster minerals are black, and porosity is white.

shocks (Figures 4b and 4e) with various mechanisms. Such healing and sealing processes modify the geometry of the stressed dissolution surface.

The healing process occurs when the aperture of the fracture remains small enough to keep some contact points between the two edges of the fracture. Mass transfer occurs (Figure 6b) from high surface energy sites (those with the highest curvature) toward low surface energy sites [*Kingery et al.*, 1976]. The process leads to the minimization of the fracture surface energy and to strengthening of the contact interface [*Renard et al.*, 2012]. Despite the fact that diffusive mass transfer occurs in a free fluid and thus over a large width of the order of magnitude of the fracture thickness, the healing process is rather slow because surface tension, that drives the process, is low. Significant healing could occur over some weeks or months depending on the solubility of the solid in solution and on the temperature that activates both the solubility and the diffusion processes [*Brantley et al.*, 1990; *Gratier and Jenatton*, 1984; *Smith and Evans*, 1984].

The sealing process is a stress-driven mass transfer process (Figure 6c). The soluble materials dissolved under the indenter (Figure 6a) or at the contact between the grains below the indenter (Figure 7a, step 3) are redeposited in the fractures and so progressively seal them. Despite the fact that the stress effect, as driving force of the sealing process, is much higher that the surface energy effect of the self-healing process (thousand times higher [*Gratier et al.*, 2013a]), the sealing process is slower than the self-healing process, because it is limited by a diffusion along the very thin fluid phase trapped under stress (some nanometer thickness). However, it is shown to occur even in the laboratory (Figures 4b and 4e). As fractures are progressively healed or sealed, they stop providing a shortcut for diffusion (Figure 6a). This leads to a progressive slow down of the displacement rate. Both processes strengthen the rocks [*Gratier*, 2011].

4.4. Effect of Changes in Dissolution Surface Roughness and Porosity

Another process that can modify the geometry of the indenter-sample interface and so explain the slowing down of the postshock displacement (Figure 2) is the evolution of the roughness of the sample. In parallel with fracture healing and sealing, the dissolution contact roughness also changes with time after the shock both for porous and nonporous materials (Figures 4 and 5). A schematic representation of this change is given in Figure 7a: just after the shock (step 1), there exist a few actual contacts between the indenter and the sample. Then, the total contact surface area increases with time due to the progressive displacement of the indenter under the effect of dissolution. Consequently, the displacement rate decreases due to its inverse

dependence on the contact area, with increasing mass transfer distance and decreasing stress [*Dewers and Ortoleva*, 1990; *Lehner*, 1995; *Renard et al*., 1999].

Moreover, for porous granular materials, such as plaster, the porosity drastically decreases in the bulk volume below the indenter (Figure 4j). The thickness of this compacted damaged zone below the indenter is of the order of magnitude of the indenter diameter. In this case, the change in creep rate is even more dramatic (Figure 2). A schematic representation of this change is given in Figure 7b. First, permanent dissolution progressively reduces the porosity (Figure 7b, steps 1 and 2). Then, the shock induces a drastic comminution process (Figure 7b, step 3). Finally, the porosity decreases progressively by pressure solution compaction. It was not possible to distinguish between the mechanisms involved in this last stage at grain scale, as grain boundary sliding, dissolution indenting (Figure 5f), and redeposition in the pores may be involved. Such behavior could be compared with the results obtained in slide-hold-slide experiments on mixtures of halite and phyllosilicate. A strongly nonlinear compaction is observed as both grain packing density and contact grain surface area increase during hold periods [*Bos and Spiers*, 2002; *Niemeijer and Spiers*, 2006]. Such studies are complementary of our work, as the hold time during which healing occurs is much shorter (hour) than that the one used in our experiment (month). During relatively short time (minutes), it could be expected that some brittle deformation occurs after the shock, but our time frequency measurements did not allow investigating such deformation mechanism.

With the dynamic indenting technique, the rheological change expected during the seismic cycle is reproduced under laboratory conditions: an instantaneous acceleration of the displacement rate is associated with fracturing and comminution processes, then a progressive slowing down of the displacement rate can be associated with a postseismic healing, here a pressure solution process that appears to be both controlling the creeping and the postseismic healing and sealing processes, as in natural deformation [*Gratier et al*., 2011].

4.5. Time-Dependent Variation in the Postshock Power Law From Experimental Data

The parameters involved in the displacement versus the time relationship merit further detailed discussion (Figure 3). The shapes of the creep curves in time windows of 100 h before and after each shock were studied. The semilog plot of Figure 3b shows that a logarithmic law does not fit the postshocks. The log-log plot in Figure 3a (top) clearly shows that such postshock curves are best fitted by power laws, with an exponent that varies between 0.3 and 0.5. Conversely, the curves before the shock show a linear trend ($n = 1$; Figure 3a, bottom) reflecting the progressive change from a nonsteady state (immediately after the shock) to a steady state creep (after the healing process effect). This steady state is reached after several hundred hours in the experiments, either after the beginning of the indenting process or after each shock (Figure 2).

The diagram in Figure 8a shows in greater detail the variation in mean displacement rate over a period of 100 h for an experiment on plaster with four successive shocks. Full and open symbols correspond to the preshock and the postshock displacements, respectively. Displacement rates increase after each shock, but the accelerating effect is progressively reduced from the first shock to the last, probably due to the decrease in porosity with time that strengthens the sample (Figure 7b). The same accelerating effect of the shock is seen for the other minerals (halite and calcite), and the accelerating effect remains similar for the three shocks, since here there is no change in porosity.

Figure 8b also shows the variation in the exponent of the power law (n) before and after the shock: full and open symbols correspond to the preshock and the postshock, respectively. For plaster, the exponent decreases from a value close to 1.0 before the shock to 0.4 after each of the four shocks and then returns to a value close to 1.0 and so on. Note that in some cases, especially when the weight of the ball was low (28 g for the first shock), the change in the value of n was not as large as when the weight of the ball was higher (80 g for the other three shocks). This is interpreted by the fact that in the first shock (28 g), the dynamic effect was not sufficiently strong to trigger a substantial change in the value of n. The value of n is seen to change in a similar fashion for the other minerals (calcite and halite), but with a greater degree of variation. Anyway, in these cases, the exponent increased during the seismic cycle from 0.4 just after the shock to 1 after the postshock healing process. Note that the power law exponent value just after the shock is close to the value of one third found by *Dysthe et al*. [2002] for static indenting experiments on undeformed halite and explained by the flattening of the initial roughness of the dissolution contact area.

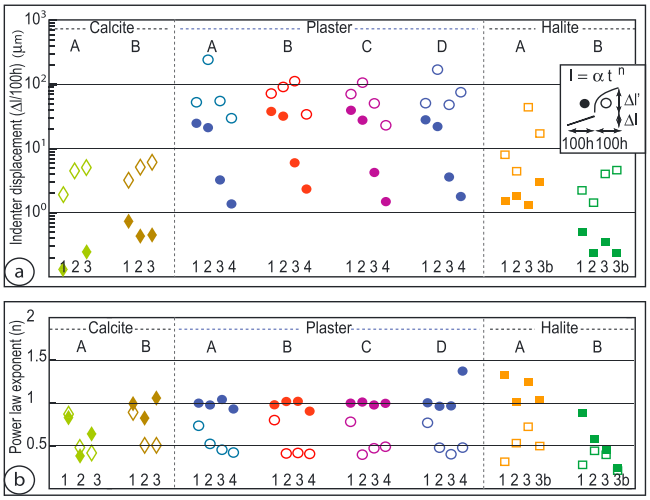

Figure 8. Variation in the parameters of the time-dependent displacement relationships: (a) Variation in mean displacement of the indenter (Δl) during a time window of 100 h for successive shocks (three for calcite and four for plaster and halite), see Figure 2; solid symbols indicate the displacement before the shock (Δl), and open symbols indicate the displacement after the shock ($\Delta l'$). (b) Variation in the power law exponents (n) during a time window of 100 h with respect to the successive shocks showing that the power law exponents increase from 0.3 to 0.5 just after the shock to 1 after several hundred hours of healing.

4.6. Time-Dependent Variation in the Postseismic Power Law From Natural Faults

This creep behavior in the experiments can be compared with the natural observations of postseismic (afterslip) creeping fault zones. Logarithmic dependence is most often found for the variation in displacement rate, for short periods (some months) and for some shallow creeping faults after an earthquake, like the 2004 *M*6 Parkfield earthquake [*Freed*, 2007]. Models including the rate-and-state friction law, based on the steady state approximation of the friction law, were also proposed to fit other data [*Marone et al*., 1991]. However, if the steady state approximation for friction is not used, the rate-and-state law may lead to much more complex behavior with afterslip decaying according to a power law of time with various characteristic times and exponents [*Helmstetter and Shaw*, 2009]. Power law models were also used to fit postseismic displacements in relation to models of viscous flow in the lower crust or in the upper mantle described by power law creep [*Freed and Bürgmann*, 2004]. Finally, exponential decay may also fit the data well, for example, using interferometric synthetic aperture radar (InSAR) and GPS data for the 2004 *M*6 Parkfield afterslip period [*Johanson et al*., 2006]. However, all these fits are also possible, because the noise level and accuracy of postseismic creep data are such that it is difficult to distinguish between logarithmic or power law dependence with time.

Working on raw data, for example, when using displacements recorded by continuous GPS measurements after the 2004 *M*6 Parkfield earthquake (Southern California Integrated GPS Network and U.S. Geological Survey (USGS)), the postseismic displacements may be fitted by one or two power laws with exponents in the range of 0.25–0.4 (Figures 9c and 9d). Similarly, the postseismic displacement after the 1999 *M*7.2–7.4 Izmit earthquake [*Cakir et al*., 2012; *Ergintav et al*., 2009; *Reilinger et al*., 2000] can be fitted with a power law with an exponent close to 0.36 (Figures 9a and 9b).

Note that the healing and sealing processes in the experiments are also observed in natural deformation. This is true for healed fractures as seen in the samples collected from the San Andreas Fault zone north of Parkfield, in the SAFOD borehole (Figures 6d and 6e). This process of fault damage recovery is commonly observed in exhumed fault zones all over the world [*Boullier et al*., 2001; *Chester and Logan*, 1986; *Cox*, 2010; *Faulkner et al*., 2010]. Sealed fractures can also be observed in the SAFOD samples, Figure 6f associated with dissolution features [*Holdsworth et al*., 2011; *Mittempergher et al*., 2011] and within numerous other faults [*Ramsay and Huber*, 1987; *Scholz*, 2002]. So the mechanisms of postseismic fault healing are identical in natural deformation and in the dynamic indenting experiments. However, the characteristic healing time is not the same because the laboratory experiments use specific materials. The main difference lies in the solubility of the solid in solution, which is 10 to 100 times greater in the experiments when using halite, gypsum (plaster), or calcite saturated with high-solubility solvent, compared to the natural material in the fault zone such as calcite, quartz, feldspars, and serpentines that are seen to be dissolved and redeposited in the presence of water [*Andreani et al*., 2005; *Gratier et al*., 2011; *Holdsworth et al*., 2011]. Characteristic healing times in laboratory experiments range from 100 to 1000 h, respectively, for nonporous or porous materials (Figure 2). Consequently, the difference with natural deformation must be 10 to 100 times higher, leading to natural

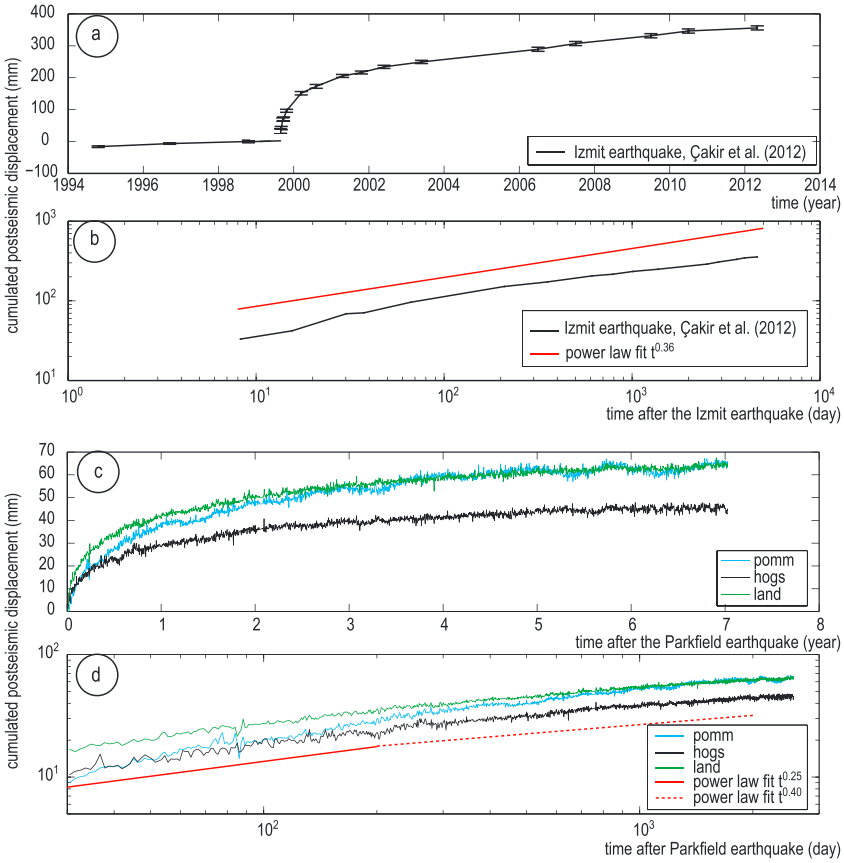

Figure 9. Time-dependent postseismic displacement and power law fits for two active faults. (a) Postseismic displacement after the 1999 *M*7.2–7.4 Izmit (Turkey) earthquake measured from GPS data [*Cakir et al.*, 2012]. The coseismic displacement has been removed. (b) In a log-log plot, the postseismic displacement shows a linear trend with time, indicative of power law dependence, with a time exponent close to 0.36. (c) Representative postseismic displacement for the 2004 *M*6 Parkfield (California) earthquake based on the continuous GPS measurements and (d) log-log plot showing power law dependence, with time exponents in the range of 0.25 to 0.4. The data from three continuous GPS measurements—pomm, land, and hogg—located near the fault are provided by the USGS.

deformation characteristic healing times ranging from several months to several dozen years, which is plausible. However, estimating the scaling between experimental data and natural rates remains challenging.

The relative proportion of strain between friction and pressure solution processes is also not easy to estimate. However, as friction processes require higher differential stress values than pressure solution [*Gratier et al.*, 2013a], friction-controlled processes must be limited to short durations after the earthquake (days to weeks) and leave place to pressure solution creep and healing processes for the long durations (months to centuries). Moreover, friction along postseismic gouge should generate heat, and this could be verified by temperature measurements in boreholes crossing active faults.

The combined effect of the change in roughness of the dissolution surface and in fracture healing most probably explains the observed power law dependence both in nature and in the experiments. In fault zones, monitoring the variation in power law parameters may provide a means of determining the characteristic healing times in seismic faults (the time of the transition from a power law to a linear evolution with time). This healing time also determines the strength of the fault, its capacity to accumulate elastic energy, stress distribution, and possibly the time to the next major earthquake.

It must be noted that this new proposed mechanism applies for afterslip behavior in seismic zones with transient (postseismic) creep. In the zone of permanent creep, microseismicity is often observed that could also activate the pressure solution creep process. However, this effect cannot be seen on the displacement rate measured at the Earth's surface. The partition between the zones of permanent creep and the zones of

transient (postseismic) creep is discussed in another study [*Gratier et al*., 2013b]. It is mostly related to the differences in lithology and geological conditions.

5. Conclusion

Using a dynamic indenting technique, experimental results demonstrate that pressure solution creep, a creep and sealing mechanism, can accommodate both steady state creep and transitory postseismic creep. During transitory postseismic creep, the same change is found both in experiments and in two continental fault zones—the San Andreas Fault at Parkfield and the North Anatolian Fault at Izmit—where postseismic displacement rates were recorded. In the experiments, just after a shock (to be compared to a natural seismic event), the postseismic displacement rate drastically increases due to the effects of fracturing and comminution processes. Fracturing reduces the mass transfer distance in the trapped fluid phase in the dissolution zone, the displacement rate being inversely proportional to the square of the mass transfer distance (or to the area of dissolution). Comminution reduces the dissolution contact area leading to a local increase in stress.

Subsequently, the postshock (or the postseismic) displacement rate gradually decreases following a power law with time due to (i) the progressive healing and sealing of the fracture, (ii) the progressive flattening of the dissolution surface roughness, and (iii) for porous material, the gradual decrease in porosity of the material below the indenter (or around the fault in natural deformation).

As a consequence, the displacement rate varies with time as follows: (i) Just after a shock (or a seismic event), the creep displacement versus time curve can be fitted by a power law, with an exponent in the range of 0.25–0.5 both in natural deformation and in the experiment. (ii) Then the displacement versus time curve shows a progressive transition from nonsteady state toward steady state creep with a linear relationship with time. This transition takes several hundred hours in the experiments. Due to the differences in the solubility of the solid in solution between natural rocks in fault zones and samples in the experiments, the transition could take from several months up to several hundred years in natural active faults. Consequently, monitoring the power law parameters of postseismic (afterslip) fault creep may provide a means of determining the characteristic healing time in the fault (the time of the transition from a power law to a linear evolution with time).

Acknowledgments

We thank Robert Holdsworth and Matt Ikari for their comments that helped to improve the manuscript. We also thank Ziyadin Çakir (Istanbul Technical University, Turkey) for sharing the InSAR data of the North Anatolian Fault and for the interesting discussions on the dynamics of postseismic creep. This study was supported by the Institut National des Sciences de l'Univers, the OSUG@2010 Labex, the NEEDS CNRS, and the FISIC ANR programs.

References

Andreani, M., A. M. Boullier, and J.-P. Gratier (2005), Development of schistosity by dissolution-crystallization in a Californian serpentinite gouge, *J. Struct. Geol.*, *27*(12), 2256–2267.

Barbot, S., Y. Fialko, and Y. Bock (2009), Postseismic deformation due to the M-w 6.0 2004 Parkfield earthquake: Stress-driven creep on a fault with spatially variable rate-and-state friction parameters, *J. Geophys. Res.*, *114*, B07405, doi:10.1029/2008JB005748.

Bos, B., and C. J. Spiers (2002), Fluid-assisted healing processes in gouge-bearing faults: Insights from experiments on a rock analogue system, *Pure Appl. Geophys.*, *159*(11–12), 2537–2566.

Boullier, A. M., T. Ohtani, K. Fujimoto, H. Ito, and M. Dubois (2001), Fluid inclusions in pseudotachylytes from the Nojima fault, Japan, *J. Geophys. Res.*, *106*(B10), 21,965–21,977.

Bradbury, K. K., J. P. Evans, J. S. Chester, F. M. Chester, and D. Kirschner (2011), Lithology and internal structure of the San Andreas fault at depth based on characterization of Phase 3 whole-rock core in the San Andreas Fault Observatory at Depth (SAFOD) borehole, *Earth Planet. Sci. Lett.*, *310*(1–2), 131–144.

Brantley, S., B. Evans, S. H. Hickman, and D. A. Crerar (1990), Healing of microcracks in quartz: Implications for fluid flow, *Geology*, *18*, 136–139.

Brenguier, F., M. Campillo, C. Hadziioannou, N. M. Shapiro, R. M. Nadeau, and E. Larose (2008), Postseismic relaxation along the San Andreas fault at Parkfield from continuous seismological observations, *Science*, *321*(5895), 1478–1481.

Cakir, Z., S. Ergintav, H. Ozener, U. Dogan, A. M. Akoglu, M. Meghraoui, and R. Reilinger (2012), Onset of aseismic creep on major strike-slip faults, *Geology*, *40*(12), 1115–1118.

Carpenter, B. M., C. Marone, and D. M. Saffer (2011), Weakness of the San Andreas Fault revealed by samples from the active fault zone, *Nat. Geosci.*, *4*(4), 251–254.

Chester, F. M., and J. M. Logan (1986), Implication for mechnical prperties of britle faults from observation of the Punchbowl fault zone, California, *Pure Appl. Geophys.*, *124*(1–2), 79–106.

Chlieh, M., J. B. de Chabalier, J. C. Ruegg, R. Armijo, R. Dmowska, J. Campos, and K. L. Feigl (2004), Crustal deformation and fault slip during the seismic cycle in the North Chile subduction zone, from GPS and InSAR observations, *Geophys. J. Int.*, *158*(2), 695–711.

Cox, S. (2010), The application of failure mode diagrams for exploring the roles of fluid pressure and stress states in controlling styles of fracture-controlled permeability enhancement in faults and shear zones, *Geofluids*, *10*(1–2), 217–233.

Dewers, T., and P. Ortoleva (1990), A coupled reaction / transport / mechanical model for intergranular pressure solution stylolites, and differential compaction and cementation in clean sandstones, *Geochim. Cosmochim. Acta*, *54*, 1609–1625.

Donnellan, A., J. W. Parker, and G. Peltzer (2002), Combined GPS and InSAR models of postseismic deformation from the Northridge earthquake, *Pure Appl. Geophys.*, *159*(10), 2261–2270.

Dysthe, D. K., Y. Podladchikov, F. Renard, J. Feder, and B. Jamtveit (2002), Universal scaling in transient creep, *Phys. Rev. Lett.*, *89*, doi:10.1103/PhysRevLett.1189.246102.

Dysthe, D. K., F. Renard, J. Feder, B. Jamtveit, P. Meakin, and T. Jøssang (2003), High resolution measurments of pressure solution creep, *Phys. Rev. E*, *68*(011603), doi:10.1103/PhysRevE.1168.011603.

Ergintav, S., S. McClusky, E. Hearn, R. Reilinger, R. Cakmak, T. Herring, H. Ozener, O. Lenk, and E. Tari (2009), Seven years of postseismic deformation following the 1999, M=7.4 and M=7.2, Izmit-Duzce, Turkey earthquake sequence, *J. Geophys. Res.*, *114*, B07403, doi:10.1029/2008JB006021.

Faulkner, D. R., C. A. L. Jackson, R. J. Lunn, R. W. Schlische, Z. K. Shipton, C. A. J. Wibberley, and M. O. Withjack (2010), A review of recent developments concerning the structure, mechanics and fluid fow properties of fault zones, *J. Struct. Geol.*, *32*, 1557–1575.

Feigl, K. L., and W. Thatcher (2006), Geodetic observations of post-seismic transients in the context of the earthquake deformation cycle, *C. R. Geosci.*, *338*(14–15), 1012–1028.

Freed, A. M. (2007), Afterslip (and only afterslip) following the 2004 Parkfield, California, earthquake, *Geophys. Res. Lett.*, *34*, L06312, doi:10.1029/102006GL029155.

Freed, A. M., and R. Bürgmann (2004), Evidence of power-law flow in the Mojave desert mantle, *Nature*, *430*(6999), 548–551.

Freed, A. M., R. Burgmann, E. Calais, and J. Freymueller (2006), Stress-dependent power-law flow in the upper mantle following the 2002 Denali, Alaska, earthquake, *Earth Planet. Sci. Lett.*, *252*(3–4), 481–489.

Gratier, J.-P. (1993), Experimental pressure solution of halite by an indenter technique, *Geophys. Res. Lett.*, *20*, 1647–1650.

Gratier, J.-P. (2011), Fault permeability and strength evolution related to fracturing and healing episodic processes (years to millennia): The role of pressure solution, *Oil Gas Sci. Technol.*, *3*, 491–506.

Gratier, J.-P., and L. Jenatton (1984), Deformation by solution - deposition and reequilibration of fluid inclusions in crystals depending on temperature, internal pressure and stress, *J. Struct. Geol.*, *5*, 329–339.

Gratier, J.-P., R. Guiguet, F. Renard, L. Jenatton, and D. Bernard (2009), A pressure solution creep law for quartz from indentation experiments, *J. Geophys. Res.*, *114*, B03403, doi:10.1029/2008JB005652.

Gratier, J.-P., J. Richard, F. S. Renard, S. Mittempergher, M. L. Doan, G. Di Toro, J. Hadizadeh, and A.-M. Boullier (2011), Aseismic sliding of active faults by pressure solution creep: Evidence from the San Andreas Fault Observatory at Depth, *Geology*, *39*(12), 1131–1134.

Gratier, J.-P., D. K. Dysthe, and F. Renard (2013a), The role of pressure solution creep in the ductility of the Earth's upper crust, *Adv. Geophys.*, *54*, 47–179.

Gratier, J.-P., F. Thouvenot, L. Jenatton, A. Tourette, M.-L. Doan, and F. Renard (2013b), Geological control of the partitioning between seismic and aseismic sliding behaviour in active faults: Evidence from the Western Alps, France, *Tectonophysics*, *600*, 226–242.

Hadizadeh, J., S. Mittempergher, J.-P. Gratier, F. Renard, G. Di Toro, J. Richard, and H. A. Babaie (2012), A microstructural study of fault rocks from the SAFOD: Implication for the deformation mechanisms and strength of the creeping segment of the San Andreas Faults, *J. Struct. Geol.*, *42*, 246–260, doi:10.1016/j.jsg.2012.04.011.

Heki, K., S. Miyazaki, and H. Tsuji (1997), Silent fault slip following an interplate thrust earthquake at the Japan Trench, *Nature*, *386*(6625), 595–598.

Helmstetter, A., and B. E. Shaw (2009), Afterslip and aftershocks in the rate-and-state friction law, *J. Geophys. Res.*, *114*, B01308, doi:10.1029/2007JB005077.

Hetland, E. A., and B. H. Hager (2005), Postseismic and interseismic displacements near a strike-slip fault: A two-dimensional theory for general linear viscoelastic rheologies, *J. Geophys. Res.*, *110*, B10401, doi:10.1029/2005JB003689.

Hickman, S. H., and B. Evans (1991), Experimental pressure solution in halite: The effect of grain/ interphase boundary structure, *J. Geol. Soc. London*, *148*, 549–560.

Holdsworth, R. E., E. W. E. van Diggelen, C. J. Spiers, J. H. P. de Bresser, R. J. Walker, and L. Bowen (2011), Fault rocks from the SAFOD core samples: Implications for weakening at shallow depths along the San Andreas Fault, California, *J. Struct. Geol.*, *33*(2), 132–144.

Hsu, Y. J., M. Simons, J. P. Avouac, J. Galetzka, K. Sieh, M. Chlieh, D. Natawidjaja, L. Prawirodirdjo, and Y. Bock (2006), Frictional afterslip following the 2005 Nias-Simeulue earthquake, Sumatra, *Science*, *312*(5782), 1921–1926.

Hsu, Y. J., S. B. Yu, and H. Y. Chen (2009), Coseismic and postseismic deformation associated with the 2003 Chengkung, Taiwan, earthquake, *Geophys. J. Int.*, *176*(2), 420–430.

Ikornikova, N. Y. (1961), The process of solution of calcite in aqueous solution of chlorides ar high temperatures and pressures, *Soviet Phys. Crystallogr.*, *5*, 726–733.

Janssen, C., R. Wirth, A. Reinicke, E. Rybacki, R. Naumann, H.-R. Hans-Rudolf Wenk, and D. Dresen (2011), Nanoscale porosity in SAFOD core samples (San Andreas Fault), *Earth Planet. Sci. Lett.*, *301*(1–2), 179–189.

Johanson, I. A., E. J. Fielding, F. Rolandone, and R. Bürgmann (2006), Coseismic and postseismic Slip of the 2004 Parkfield Earthquake from Space-Geodetic Data, *Bull. Seismol. Soc. Am.*, *96*, doi:10.1785/0120050818.

Jonsson, S., P. Segall, R. Pedersen, and G. Bjornsson (2003), Post-earthquake ground movements correlated to pore-pressure transients, *Nature*, *424*(6945), 179–183.

Karcz, Z., E. Aharonov, D. Ertas, R. Polizzotti, and C. H. Scholtz (2006), Stability of a sodium chloride indenter contact undergoing pressure solution, *Geology*, *34*, 61–63.

Karcz, Z., E. Aharonov, D. Ertas, R. Polizzotti, and C. H. Scholz (2008), Deformation by dissolution and plastic flow of a single crystal sodium chloride indenter: An experimental study under the confocal microscope, *J. Geophys. Res.*, *113*, B04205, doi:10.1029/02006JB004630.

Kingery, W. D., H. K. Bowen, and D. R. Ulhmann (1976), *Introduction to Ceramics*, 2nd ed., 1032 pp., Wiley-Interscience, John Wiley, New York.

Kreemer, C., G. Blewitt, and F. Maerten (2006), Co- and postseismic deformation of the 28 March 2005 Nias M(w) 8.7 earthquake from continuous GPS data, *Geophys. Res. Lett.*, *33*, L07307, doi:10.1029/2005GL025566.

Langbein, J., et al. (2005), Preliminary report on the 28 September 2004, M 6.0 Parkfield, California earthquake, *Seismol. Res. Lett.*, *76*(1), 10–26.

Lehner, F. K. (1995), A model for intergranular pressure solution in open systems, *Tectonophysics*, *245*, 153–170.

Li, Y. G., P. Chen, E. S. Cochran, J. E. Vidale, and T. Burdette (2006), Seismic evidence for rock damage and healing on the San Andreas fault associated with the 2004 M 6.0 Parkfield earthquake, *Bull. Seismol. Soc. Am.*, *96*(4), 349–363.

Lockner, D. A., C. Morrow, D. Moore, and S. Hickman (2011), Low strength of deep San Andreas fault gouge from SAFOD core, *Nature*, *472*(7341), 82–U107.

Marone, C. (1998), Laboratory-derived friction laws and their application to seismic faulting, *Annu. Rev. Earth Planet. Sci.*, *26*, 643–696.

Marone, C., C. H. Scholtz, and R. Bilham (1991), On the mechanism of earthquake afterslip, *J. Geophys. Res.*, *96*(B5), 8441–8452.

Mittempergher, S., G. Di Toro, J.-P. Gratier, J. Hadizadeh, S. A. F. Smith, and R. Spiess (2011), Evidence of transient increases of fluid pressure in SAFOD phase III cores, *Geophys. Res. Lett.*, *38*, L03301, doi:10.1029/2010GL046129.

Moore, D., and M. J. Rymer (2012), Correlation of clayey gouge in a surface exposure of serpentinite in the San Andreas Fault with gouge from the San Andreas Fault Observatory at Depth (SAFOD), *J. Struct. Geol.*, *38*, 51–60.
Nadeau, R. M., A. Michelini, R. A. Uhrhammer, D. Dolenc, and T. V. McEvilly (2004), Detailed kinematics, structure and recurrence of microseismicity in the SAFOD target region, *Geophys. Res. Lett.*, *31*, L12S08, doi:10.1029/2003GL019409.
Niemeijer, A. R., and C. J. Spiers (2006), Velocity dependence of strength and healing behaviour in simulated phyllosilicate-bearing fault gouge, *Tectonophysics*, *427*(1–4), 231–253.
Nur, A., and J. Booker (1972), Aftershocks cause by pore-fluid flow?, *Science*, *175*, 885–887.
Paterson, M. S. (1973), Nonhydrostatic thermodynamics and its geologic applications, *Rev. Geophys. Space Phys.*, *11*, 355–389.
Perfettini, H., and J.-P. Avouac (2004), Postseismic relaxation driven by brittle creep: A possible mechanism to reconcile geodetic measurements and the decay rate of aftershocks, application to the Chi-Chi earthquake, Taiwan, *J. Geophys. Res.*, *109*, B02304, doi:10.1029/2003JB002488.
Raj, R. (1982), Creep in polycrystalline aggregates by matter transport through a liquid phase, *J. Geophys. Res.*, *87*, 4731–4739.
Ramsay, J. G., and M. I. Huber (1987), *The Techniques of Modern Structural Geology. Volume 2: Folds and Fractures*, 700 pp., Academic Press, London.
Reilinger, R. E., et al. (2000), Coseismic and Postseismic Fault Slip for the 17 August 1999, M = 7.5, Izmit, Turkey Earthquake, *Science*, *289*(5484), 1519–1524.
Renard, F., A. Park, P. Ortoleva, and J.-P. Gratier (1999), An integrated model for transitional pressure solution in sandstones, *Tectonophysics*, *312*(2–4), 97–115.
Renard, F., S. Beaupretre, C. Voisin, D. Zigone, D. Candela, D. K. Dysthe, and J.-P. Gratier (2012), Strength evolution of a reactive frictionnal interface: An analogue experiment, *Earth Planet. Sci. Lett.*, *341-344*(20–34), doi:10.1016/j.epsl.2012.1004.1048.
Richard, J., J.-P. Gratier, M. L. Doan, F. Renard, and A. M. Boullier (2013), Time and space evolution of an active creeping zone: Competition between brittle and ductile deformations, new insights from microstructure studies of SAFOD (San Andreas Fault Observatory at Depth) samples, *EGU General Assembly*, *Vienna*, *Austria*, 7–12 April, id. EGU2013-1422.
Rutter, E. H. (1976), The kinetics of rock deformation by pressure solution, *Philos. Trans. R. Soc. London*, *283*, 203–219.
Schleicher, A. M., L. N. Warr, and B. A. V. van der Pluijm (2009), On the origin of mixed-layered clay minerals from the San Andreas Fault at 2.5-3 km vertical depth (SAFOD drillhole at Parkfield, California), *Contrib. Mineral. Petrol.*, *157*(2), 173–187.
Scholz, C. H. (2002), *The Mechanics of Earthquakes and Faulting*, 2nd ed., 471 pp., Cambridge Univ. Press, Cambridge, U. K.
Sieh, K. E. (1978), Slip along San Andreas fault associated with great 1857 earthquake, *Bull. Seismol. Soc. Am.*, *68*(5), 1421–1448.
Smith, D. L., and B. Evans (1984), Diffusional crack healing in quartz, *J. Geophys. Res.*, *89*, 4125–4135.
Spencer, J. Q. G., J. Hadizadeh, J.-P. Gratier, and M. L. Doan (2012), Dating deep? Luminescence studies of fault gouge from the San Andreas Fault Zone 2.6 km beneath Earth's surface, *Quat. Geochronol.*, *10*, doi:10.1016/j.quageo.2012.1004.1023.
Tada, R., and R. Siever (1986), Experimental knife-edge pressure solution of halite, *Geochim. Cosmochim. Acta*, *50*, 29–36.
van Noort, R., C. J. Spiers, and G. M. Pennock (2008), Compaction of granular quartz under hydrothermal conditions: Controlling mechanisms and grain boundary processes, *J. Geophys. Res.*, *113*, B12206, doi:10.1029/2008JB005815.
Weyl, P. K. (1959), Pressure solution and the force of crystallization: A phenomenological theory, *J. Geophys. Res.*, *64*, 2001–2025.
Yu, S. B., Y. J. Hsu, L. C. Kuo, H. Y. Chen, and C. C. Liu (2003), GPS measurement of postseismic deformation following the 1999 Chi-Chi, Taiwan, earthquake, *J. Geophys. Res.*, *108*(B11), 2520, doi:10.1029/2003JB002396.
Zoback, M., S. Hickman, and W. Ellsworth (2010), Scientific drilling into the San Andreas Fault Zone, *Eos, Trans. Amer. Geophys. Union* , *91*(22), 197–199.